

# The influence of X-ray coherence length on TXRF and XSW and the characterization of nanoparticles observed under grazing incidence of X-rays

Alex von Bohlen,<sup>\*a</sup> Markus Krämer,<sup>b</sup> Christian Sternemann<sup>c</sup> and Michael Paulus<sup>c</sup>

Received 2nd July 2008, Accepted 18th February 2009

First published as an Advance Article on the web 10th March 2009

DOI: 10.1039/b811178b

An approach to the chemical characterization and a study of the morphology of very fine fractions of nanoparticles on surfaces can be deduced from experiments using the grazing incidence X-ray Standing Waves (XSW) by means of Total Reflection X-ray Fluorescence (TXRF). Some theoretical aspects not considered until now for TXRF and XSW, *e.g.* the influence of coherence length of X-rays from different X-ray sources, the particle form, particle size and distribution, are presented and discussed. Results of numerical simulations of XSW-scans considering the modelling of particles are compared with the experimental data obtained from XSW experiments performed at a synchrotron radiation facility. Advantages and limitations of the applied techniques are discussed for the characterization of Au- and CdTe-nanoparticles.

## Introduction

Particles, especially the sub-micrometer size, are nowadays of great interest. They are used in many disciplines and in various applications in biology, medicine, biochemistry, pharmacy, material sciences and also in conservation sciences. Nanoparticles, in terms of diameter, are particles in the range below one micrometer. Single members of the finest fractions, those below 100 nm, are difficult to characterize by conventional methods of chemical analysis or microscopy if their morphology should not be altered.

Man is continuously producing nanoparticles. Laser printers, copy machines, diesel fuel driven cars, Pt–Pa–Rh catalyst converters built-in in cars, laser applications in medicine and technology, lasers used for Laser Induced Breakdown Spectroscopy and various other applications generate nanoparticles. These particles are suspended in air without being deposited anywhere. They remain suspended in the atmosphere and have the properties of aerosols. That means that these materials reach our lungs in an unfiltered form and our organism is able to incorporate the small fractions in the range between 1 and 20 nm diameter directly into our circulatory system. A general increasing interest is based on the mobility and activity of nanoparticles in the atmosphere, their long life time when suspended in air or in liquids and on their impact on the eco-system. Further, the catalytic potential of nanoparticles for several industrial applications is impressing. Additionally, nanoparticles are considered to be useful as ‘nanomarkers’ for single cells. Therefore, a sensitive and non-consuming characterization of

small amounts of nanoparticles deposited on surfaces would be advantageous.

A promising technique for the characterization of nanoparticles on surfaces could be the X-ray standing waves (XSW) method in grazing incidence geometry.<sup>1–5</sup> The method offers an extremely fine dynamic gauge for measuring tiny objects deposited on top of a surface or for the characterization of narrow layered systems<sup>6,7</sup> without consuming the sample. Using fluorescence detection of heavier elements ( $Z \geq 14$ ) contained in the sample their distribution perpendicular to the reflection plane should be accessible. In the present investigation some theoretical considerations concerning the total reflection of X-rays used for XSW and the detection of small particulate matter deposited on a reflector's surface irradiated by X-rays under grazing incidence conditions are presented. Further, the application of the XSW-technique to particle analysis is discussed and some results of nanoparticle measurements are included.

## The method

Total reflection of X-rays has been known for a long time.<sup>8</sup> However, the use of the phenomenon of total reflection of X-rays on a smooth surface for instrumental analytical chemistry was first introduced in 1971 by Yoneda and Horiuchi.<sup>9</sup> About 1000 original papers dealing with TXRF were published in the last four decades.<sup>10</sup> From a more general point of view, TXRF is a static method of X-ray fluorescence using a fixed angle under grazing incidence of the primary beam.<sup>1</sup> Excellent reviews dealing with theory, applications and state of the art of TXRF are available.<sup>11–15</sup> Here only some essential features of the method will be listed and discussed under a new point of view.

The most exciting topic of total reflection of X-rays on a flat surface is the existence of a field of interference produced in the triangular intersection of the incoming and totally reflected wave.<sup>14</sup> The volume above the surface of the reflector is intersected by a system of fringes, nodes and antinodes, showing

<sup>a</sup>Institute for Analytical Sciences, ISAS Dortmund Bunsen-Kirchhoff-Str. 11, 44139 Dortmund, Germany. E-mail: vonbohlen@isas.de

<sup>b</sup>Osaka Electro-Communication University, Hatsu-cho, Neyagawa, Osaka, 572-8530, Japan

<sup>c</sup>Fakultät Physik | DELTA, TU Dortmund Maria-Goeppert-Mayer Str. 2, 44221 Dortmund, Germany

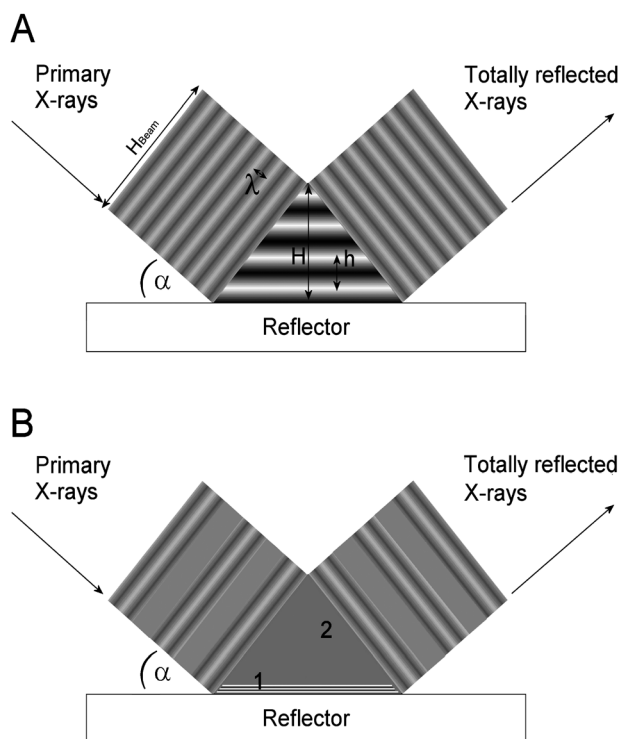


**Fig. 1** A) The usual representation of the intersection area of primary and totally reflected X-rays above a flat and even surface of a reflector. The angle  $\alpha$  is supposed to be below the critical angle of total reflection of the reflector for the wavelength  $\lambda$ . The intersection is completely interpenetrated by interference fringes. B) The same situation if considering the finite coherence length of the X-ray beam. Only a small volume close above the reflector's surface contains interference fringes (1), the major part is filled by non-modulated double intensity of the non-interfering exciting and totally reflected X-rays (2).

a periodically distributed intensity oscillation of X-ray intensity parallel to the reflection plane. The intensity varies periodically from zero to four times the intensity of the incident beam from nodes to antinodes. The number and the density of the fringes increase with the angle of incidence. However, on average a double intensity for the excitation to X-ray fluorescence is available (Fig. 1 A). In contrast to the well-known effective excitation of X-ray fluorescence in conventional (static) TXRF of materials deposited on a reflector's surface grazing incidence XSW make use of the specific information produced by the modulated field of interference.

Until now the prism-shaped intersection volume of the incoming and of the reflected wave was assumed to be filled completely with interference fringes. Considering the geometry, the wavelength  $\lambda$ , the height of the primary beam  $H_{\text{Beam}}$  and the material properties, the height  $H$  of the triangle (cut plane of the prism) can be calculated by<sup>7</sup>

$$H = \frac{H_{\text{Beam}}}{2\cos(\alpha)} \approx \frac{1}{2} H_{\text{Beam}} \quad (1)$$

For small angles, the period  $h$  of the interference fringes in the volume is given by

$$h = \frac{\lambda \sin(\alpha)}{1 - \cos(2\alpha)} \approx \frac{\lambda}{2\alpha} \quad (2)$$

A limited number of fringes in the intersection of primary and totally reflected X-rays due to the finite coherence length of light was not considered, which would result in a coherence volume smaller than the intersection volume described above.

For the TXRF device (Extra II, Rich. Seifert & Co., Ahrensburg, Germany) in our laboratory operated with a Mo-X-ray tube (using Mo  $K\alpha$ ,  $\lambda = 0.0711$  nm as the main contribution of radiation), with an incident angle of  $0.07^\circ$  for the primary X-ray beam, and a beam height of  $40 \mu\text{m}$ , the calculated values are  $H = 20 \mu\text{m}$  and  $h = 29$  nm, respectively. Thus, we expected about 690 fringes. This is not the case for a real X-ray source. For a natural width of an X-ray K line with  $\Delta E \approx 0.15$  eV or  $\Delta\lambda \approx 6.4 \times 10^{-7}$  nm ( $\Delta\lambda/\lambda \approx 9 \times 10^{-6}$ ) a longitudinal coherence length  $\xi_l \approx 4 \mu\text{m}$  is obtained according to<sup>16</sup>

$$\xi_l = \frac{\lambda}{2} \cdot \frac{\lambda}{\Delta\lambda} \quad (3)$$

The ideal (theoretical) value for the longitudinal coherence length of the Mo  $K\alpha$  excitation differs from the real value due to the use of reflectors and windows for cutting-off large parts of the radiation emitted from an X-ray tube leading to a  $\Delta\lambda/\lambda$  value not better than  $10^{-4}$ , possibly only  $10^{-3}$  or less. The value for  $\xi_l$  should not exceed  $1 \mu\text{m}$ . Modern high brilliance reflectors (multi-layer structures) used *e.g.* for SR-TXRF produced with a  $\Delta\lambda/\lambda \sim 10^{-2}$  give a longitudinal coherence length of only a few nm. Quasi-monochromatic X-rays from synchrotron radiation produced by X-ray monochromators typically have a spectral resolution of  $\Delta\lambda/\lambda \approx 10^{-4}$  resulting in a coherence length of  $\xi_l \approx 350$  nm.

The degree of transversal (spatial) coherence depends on the experimental conditions, *e.g.* the slit width ( $d_s$ ) limiting the X-ray beam in the experimental set-up and the distance slit/sample ( $R_s$ ), and on the X-ray source. Typical values of  $\xi_t$  are of the order of  $\xi_t \approx 200$  nm or  $\xi_t \approx 500$  nm, respectively, and can be achieved for *e.g.*  $\lambda = 0.0711$  nm according to<sup>16</sup>

$$\xi_t = \frac{\lambda}{2} \cdot \frac{R_s}{d_s} \quad (4)$$

As an example, the TXRF device was operated with an X-ray tube,  $R_s = 150$  mm and  $d_s = 40 \mu\text{m}$  was fixed by the manufacturer, while *e.g.*  $R_s = 1000$  mm was chosen and the slit width  $d_s$  was adjusted to  $100 \mu\text{m}$  for a synchrotron source resulting in  $\xi_t = 130$  nm and  $\xi_t = 350$  nm, respectively. That means that only a small volume above the reflector is filled with interference fringes. Thus, according to Eq. (1), using  $H_{\text{Beam}} = \xi_t$  for  $\lambda = 0.0711$  nm and an incident angle of  $0.07^\circ$ , the number of fringes was calculated to be 5 and 12, respectively. The upper part of the volume is irradiated without any modulation (*cf.* Fig. 1 B). However, it is passed once by the incoming and once by the totally reflected X-rays. Thus, a double intensity of fluorescence without modulation is excited here. On the other hand excitation generated by modulated radiation in the region just above the reflector the intensity is double only in average.

The modulated intensity distribution above the reflector can be used as an extremely fine dynamic ruler for the characterization of the smallest layers and particles, if we are able to change the angle of incidence of the primary beam continuously with sufficient accuracy and good repeatability. For this task a goniometer with at least an angle step-size not more than of  $0.001^\circ$  with

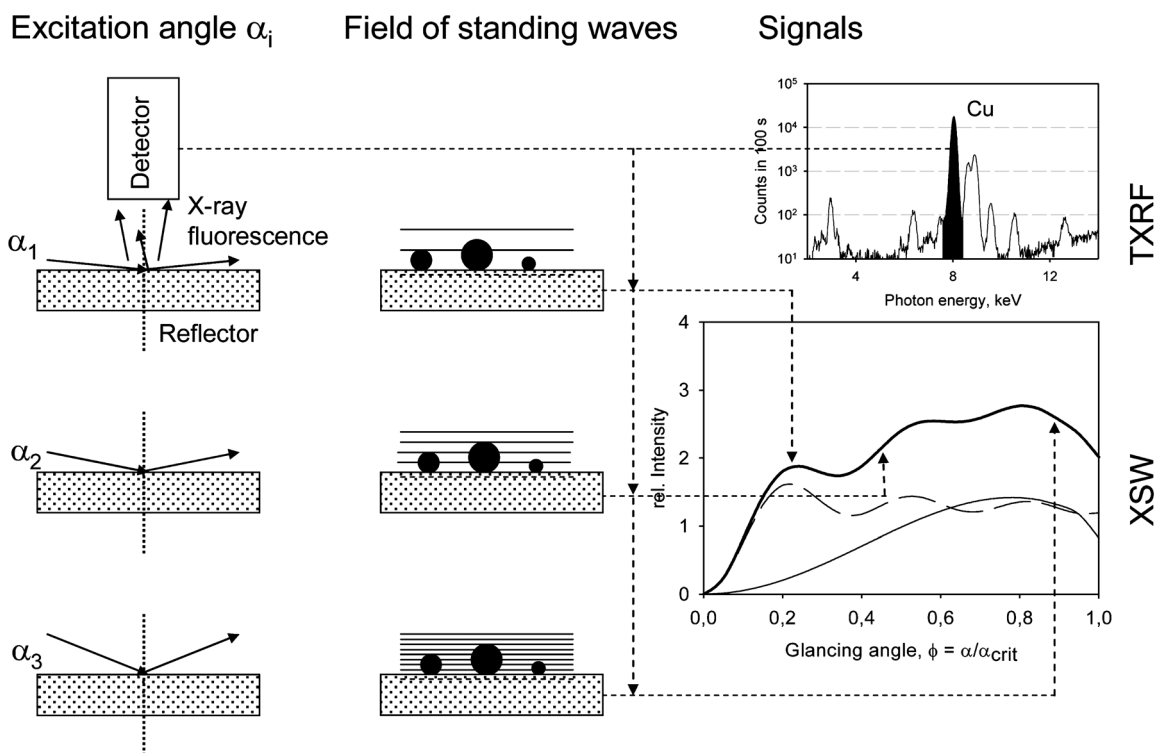


Fig. 2 Schematic representation of the principles of Total reflection X-ray fluorescence (TXRF) and of X-ray Standing Waves (XSW).

a repeatability of  $0.0005^\circ$  in the range between  $\alpha = -0.1^\circ$  and  $\alpha = 1^\circ$  is mandatory. The negative value is indispensable for exactly adjusting the zero-position in which the incident beam is parallel to the reflector surface. If we record X-ray fluorescence signals of one or more elements contained in the sample during the angle scan and then plot recorded intensities vs. angle of incidence of the primary radiation, oscillating curves are obtained (Fig. 2). This method is called Grazing Incidence X-ray Standing Waves (GIXSW) and is a combined procedure of (the static) TXRF with continuous variation of the glancing angle of the primary beam.

### Particles on a surface

According to Klockenkämper<sup>11</sup> the intensity of the radiation in a wave field is obtained by squaring the electrical field density for each position in the field. A special case of the general form presented by Bedzyk<sup>17</sup> describes only the wave field above a flat reflector with a reflectivity  $r < 100\%$ . The theory describing the interaction of the field of standing waves and particles deposited at the surface of a reflector is only valid if interferences of a small number of particles can be neglected. The equation is extended here by a layer form function  $F_i(z)$  (two examples are shown in equation (5a) for thin layered islands and small spheres) and is given by

$$I_{\text{int}}(\alpha, z) = I_0 [1 + R(\alpha) + 2\sqrt{R(\alpha)} \cos(2\pi z/a - \phi(\alpha))] \cdot F_i(z) \quad (5)$$

$$\begin{aligned} F_E(z) &= E \text{ for } z \leq E, \text{ 0 for } z > E; \\ F_s(z) &= [4z(D-z)/D^2] \text{ for } z \leq D, \text{ 0 for } z > D \end{aligned} \quad (5a)$$

where  $E$  is the height of an island,  $D$  is the diameter of a particle,  $I_0$  is the intensity of the exciting radiation (assumed to be constant in space and time),  $R(\alpha)$  describes the reflectivity of the surface in dependence on the angle  $\alpha$  and is the contribution of the reflected radiation,  $z$  is the distance perpendicular to the reflection plane. The third term contains the information of the displacement or period of the interference perpendicular to the reflection plane with  $a = \lambda/(2\sin\alpha)$  and phase-shift  $\phi$  for angles below the critical angle of total reflection  $\alpha_{\text{crit}}$  that can be calculated according to<sup>11</sup>

$$\phi(\alpha) = \arccos[2(\alpha/\alpha_{\text{crit}})^2 - 1] \quad (6)$$

where  $\phi$  decreases from  $\pi$  to 0 when  $\alpha$  increases from 0 to  $\alpha_{\text{crit}}$ . For angles  $\alpha > \alpha_{\text{crit}}$  the phase-shift  $\phi$  is always zero. The intensity

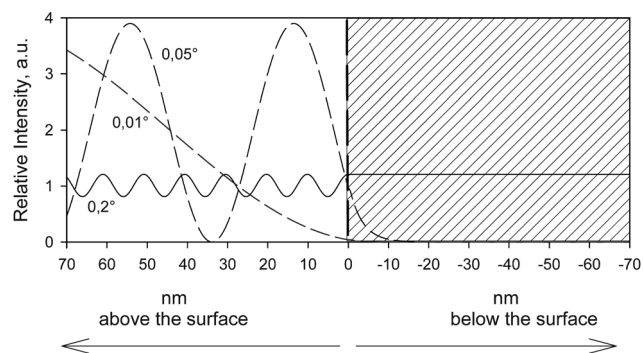
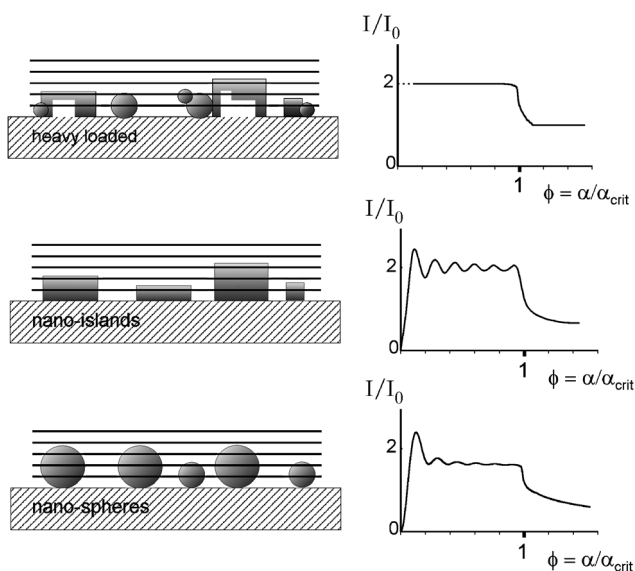


Fig. 3 X-ray standing waves above a totally reflecting surface calculated for X-ray Mo  $K\alpha$  radiation and silicon dioxide ( $\text{SiO}_2$ ) as reflector. For this combination the critical angle of total reflection is 10.2 min of arc. The reflectivity was supposed to be 1.



**Fig. 4** Three different models for top) a heavy loaded sample composed of particles of different shapes and sizes, middle) for nano-islands, and bottom) for nano-spheres subjected to XSW-scans. A detailed explanation is given in the text.

$I_{\text{int}}$  (Eq. (5)) is independent of  $x$  and  $y$  (parallel to the surface of the reflector), but dependent on the incident angle  $\alpha$  and also on the height  $z$  (perpendicular to the reflecting surface). The intensity distribution for an undisturbed interference field above, at the surface, and below the surface is shown in Fig. 3 for  $\alpha = 0.01^\circ$ , for  $0.05^\circ$ , and for  $0.2^\circ$ , respectively. For all angles below the critical angle of total reflection and an ideal surface with a reflectivity  $R(\alpha) = 1$  the intensity  $I_{R(\alpha)}$  varies between zero at the nodes and four at the antinodes. For reflectivity values  $0 < R(\alpha) < 1$  intensities  $0 < I_{R(\alpha)} < 4$  are observed. Additionally, the penetration of the radiation into the substrate according to the probability density function can be observed as an evanescent wave with a fast decay of intensity. For angles above  $\alpha_{\text{crit}}$  the radiation penetrates the substrate (Fig. 3, case with  $0.2^\circ$  calculated for Mo K $\alpha$  radiation and Si as reflector material).

Three models illustrate the differences between calculated XSW-scans (Eq. 5) for samples deposited on a flat surface of a reflector for i) a heavy loaded sample composed of particles of different shapes and sizes, ii) for randomly distributed nano-islands and iii) for spherical nanoparticles also randomly distributed on the reflectors surface. In the first case (Fig 4, top right) a horizontal line of double intensity for the angles smaller than the critical angle of total reflection was calculated while the intensity of fluorescence is only one for angles above the critical angle. This reflects the well known behaviour of TXRF.<sup>1</sup> The two following models result in oscillating XSW-scans for angles

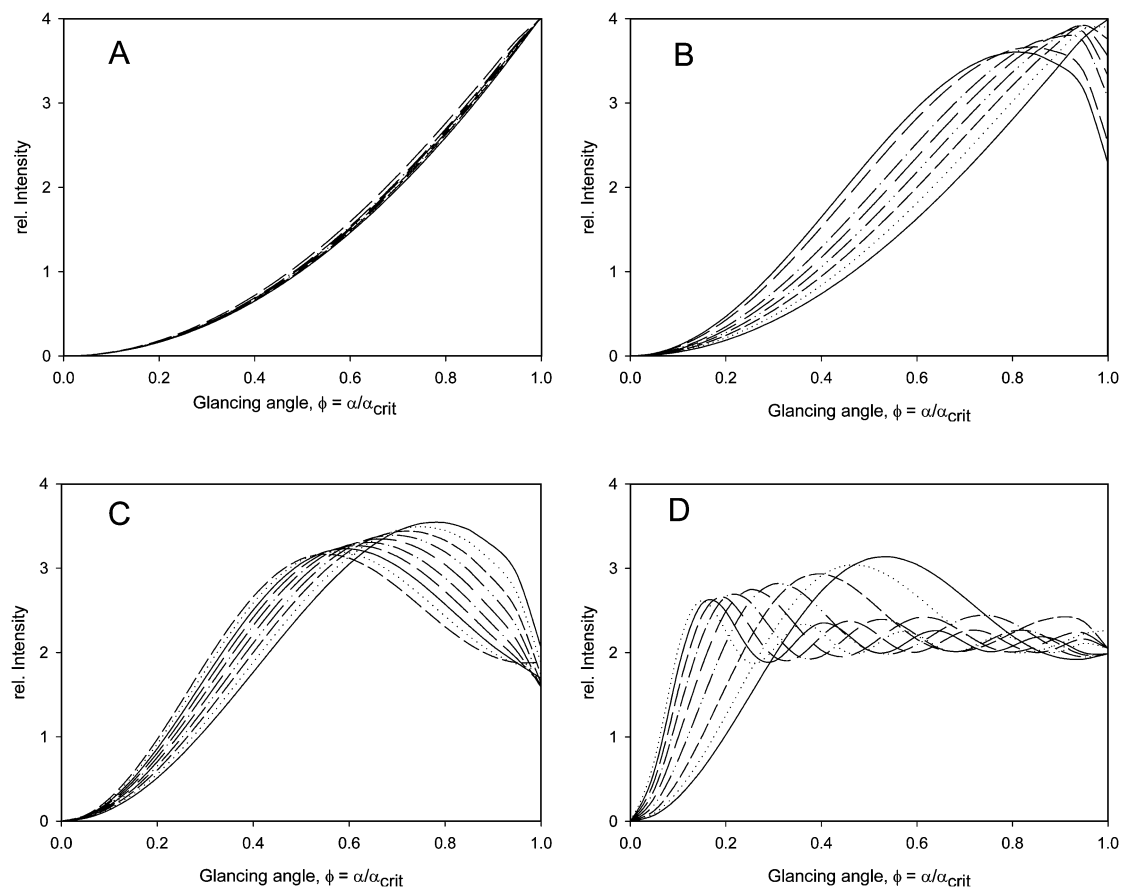


**Fig. 5** Calculated shape of XSW-signals for different sizes of nano-islands: A) 0.1–1 nm, B) 1–10 nm, C) 10–20 nm and D) 30–100 nm according to equation (5).

below the critical angle of total reflection. The oscillation is stronger for the nano-islands (Fig. 4 centre) and less strong for the spherical particles. The three models were calculated according to equation (5) based on Si as reflector and a primary radiation of 17.44 keV. Further, for the two models of nano structures a mono disperse distribution of particles and a constant total mass homogeneously distributed in the observed area was assumed. These two models were not confirmed experimentally until now. Calculated XSW signals for different heights of small islands are represented in Fig. 5. Similar curves are obtained by XSW simulations for scans of nanoparticles if they are made of a single element.

Small islands in terms of their height or particles with small diameters are not excited as efficiently as bigger ones. This is a consequence of the sinusoidal energy distribution of the excitation by the interference field. If we normalize the abscissa  $\alpha/\alpha_{\text{crit}}$  and take into account that below the critical angle the fluorescence signal is double compared to that achieved by excitation above the critical angle,<sup>1</sup> the integral of the area below the curves is 2 in accordance with general calculations for TXRF.<sup>4</sup> Unfortunately, this value is not reached for very small size fractions of nanoparticles or nano-islands. The respective value of the integral below the curves for small nanoparticles (Fig. 5A and 5B) is significantly below 2 due to an incomplete illumination by only a tail of the sinusoidal energy distribution of the interference field. This is obvious when regarding that for each angle-scan the arrival of the first antinode at the surface of the reflector coincides with the critical angle of total reflection (*cf.* Fig. 3). The results of calculated sensitivities for nano-islands in dependence of the height of the island and for different excitation energies of the primary X-rays are given in Fig. 6.

The combined influence of the longitudinal and transversal coherence length of the exciting beam on the XSW signals is shown in Fig. 7. The simulation of the XSW signals for 120 nm nano-islands and different coherence conditions shows a progress of degradation of the signal when diminishing the coherence length. The presence of the non-modulated double excitation dominates the signals and the modulated proportion loses

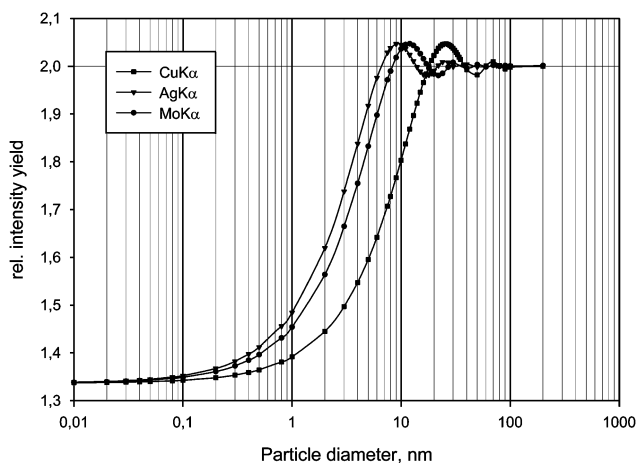


**Fig. 6** Calculated XSW intensities for islands of different heights are represented in dependence on the glancing angle of the primary excitation and on the particle sizes. Narrow objects are not excited as strongly as bigger ones.

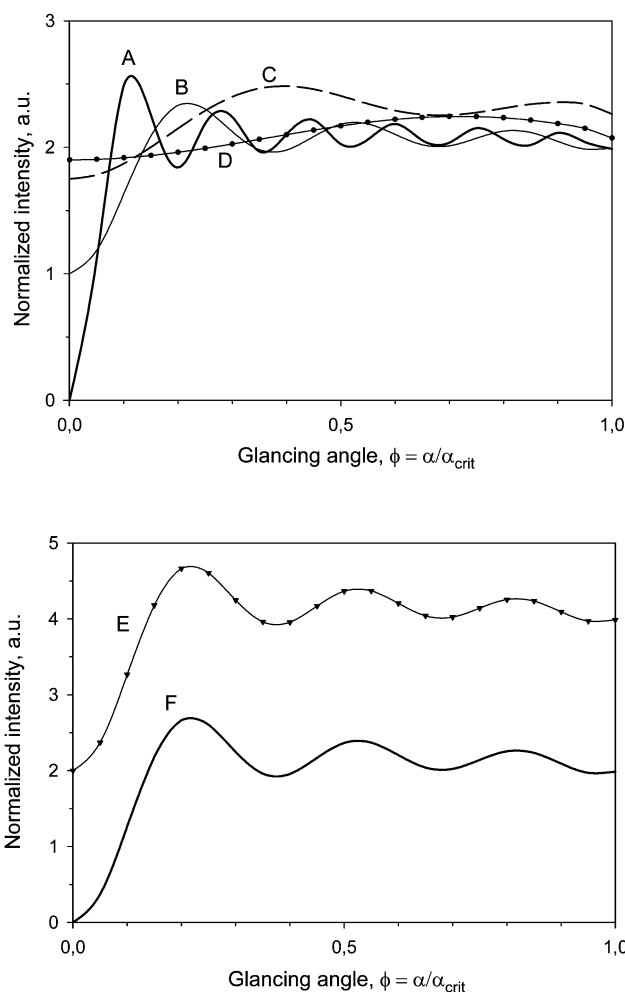


**Fig. 7** Influence of the longitudinal and transversal coherence length of primary X-rays on the XSW signal for nano-islands. Simulation for islands of 120 nm height intersected by an interference field of more than 120 nm height (A), of 60 nm interference combined with a 60 nm non-modulated excitation above the interference field (B), of 30 nm interference combined with 90 nm (C), and of 12 nm interference field combined with 108 nm excitation without modulation (D) are shown in the top part (variable excitation, constant sample). The XSW signals of 120 nm (E) and 60 nm (F) nano-islands excited by a 60 nm interference field combined with a 60 nm non-modulated excitation above the interference field are shown in the bottom part (constant excitation, variable sample height).

influence. Intensities were composed to an  $I_{\text{tot}} = I_{\text{coh}} + I_{\text{incoh}}$  where  $I_{\text{coh}} = I_{\text{inf}}$  ( $a, z < z_{\text{coh}}$ ) and  $I_{\text{incoh}} = 2I_0$  ( $a, z > z_{\text{coh}}$ ) as calculated in Eq. (5) using  $z_{\text{coh}}$  as the height of the coherence field. This suggests the existence of fractions containing only islands of very small height. Additionally, the excitation generates higher signals at very low glancing angles, *i.e.* between 0 and 0.1 times  $\alpha_{\text{crit}}$ , as can be observed in Fig. 7. Examples of XSW signals for a 120 nm height undisturbed interference field covering the full height of the sample as well as signals produced by restricting the coherence length to produce modulated interference fields of 60 nm, 30 nm and 12 nm height and replacing the excitation above the interference field by a non-modulated field of X-ray excitation (variable coherence and constant sample

height) are represented and are marked A, B, C, and D, respectively in Fig. 7 top. A comparison of simulations for constant coherence and variable sample height is presented in Fig. 7 bottom. The calculated undisturbed XSW excitation of 60 nm high islands (F) and the combined excitation of 120 nm high islands with a 60 nm height interference field and a non-modulated excitation above the interference field (E) illustrate the difference of the XSW signals.

## Matrix effects

In X-ray spectrometry matrix effects are effects concerning absorption and secondary excitation affecting the fluorescence radiation emerging from the sample after excitation by a primary radiation. The effects are strongly dependent on the matrix composition, the element to be analysed and on the thickness of the sample. Fortunately, these effects are negligible for TXRF if sample mass and thickness are below certain limits. Klockenkämper and von Bohlen calculated the tolerable limits for three different systems.<sup>18</sup> The reported upper limits for organic materials, for mineral matrices and for metals are 10  $\mu\text{m}$ , 1  $\mu\text{m}$ , and 2 nm for the thickness and 100  $\mu\text{g}$ , 1  $\mu\text{g}$ , and 0.2  $\mu\text{g}$  for the mass, respectively. Values are given for 1  $\text{cm}^2$ .

Rough-textured samples showing a homogeneous distribution and smaller dimensions than those calculated by Klockenkämper

and von Bohlen can be regarded as infinitely thin for TXRF and the analysis free of matrix effects. Later, Hellin *et al.* demonstrated the existence of matrix effects after drying liquid samples. The remaining non-homogeneously distributed residua lead to deviations in the quantification of TXRF analysis which could be corrected when considering matrix effects. They also performed angle dependent scans obtaining some hints about the morphology and distribution of the residua on the TXRF reflectors.<sup>19</sup>

For nanoparticles, especially those made of metals, severe matrix effects have to be suspected. Metallic smears considered in ref. 18 deliver negligible contribution of matrix effects only below 2 nm height. A reliable quantification of the elements contained in an alloy by means of the traditional quantification *via* internal standard for TXRF cannot be recommended. Matrix matched quantification will be necessary. The difficulties of such a procedure are immanent to the nature of nanoparticles: they have large surfaces compared to their volumes. This fact makes nanoparticles very reactive in terms of oxidation, corrosion and in general as catalytic agents.

## Experimental

XSW measurements were carried out at the DELTA Synchrotron facility Dortmund. The storage ring was operated at

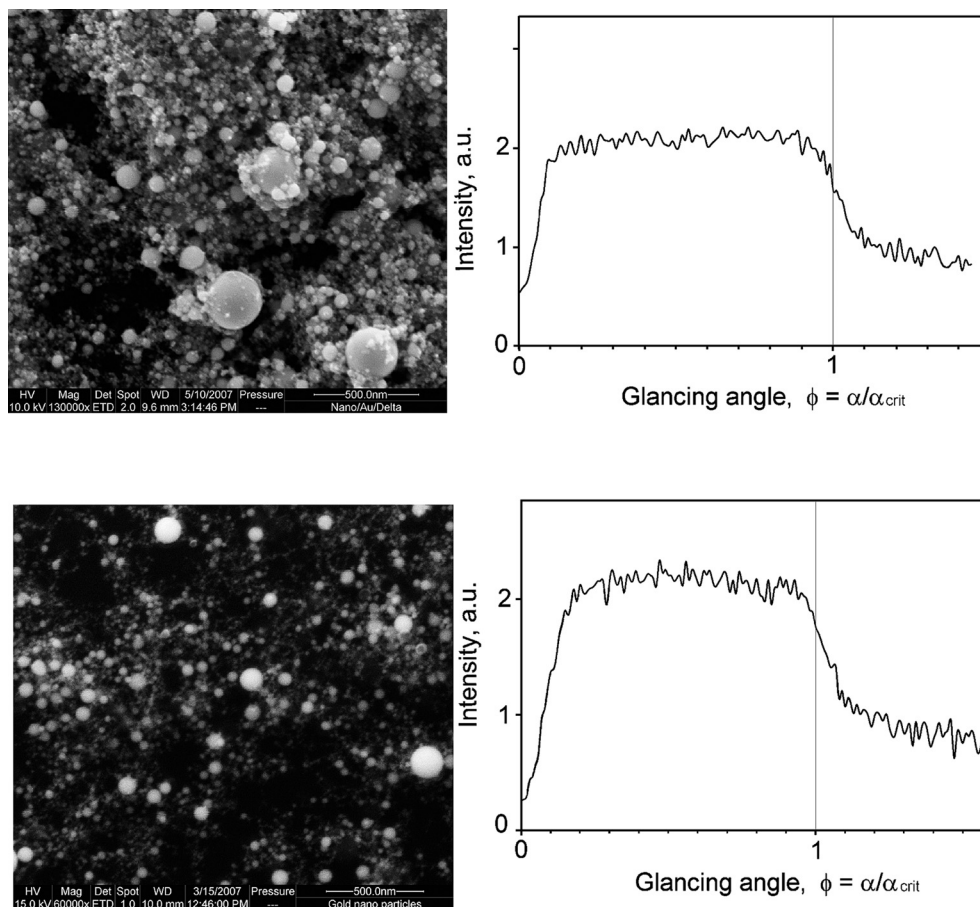


**Fig. 8** Au nanoparticles produced by fs-laser ablation with high fluence (top) and with moderate fluence (bottom). The XSW scans reveal a more or less covered reflector surface leading to a non-specific XSW signal for spherical particles.

1.5 GeV and a maximum current of 130 mA. The primary radiation was supplied by BL 9<sup>20</sup> derived from an asymmetric superconducting wiggler with a critical energy of 7.9 keV. The monochromatic radiation was selected using a double crystal monochromator equipped with a pair of Si #311 Bragg crystals. The energy resolution is of the order of  $\Delta E/E = 10^{-4}$ , the photon flux about  $10^9$  photons  $s^{-1}$  and the energy range can be tuned from 5 to 30 keV. The angle scans were performed at a 6-circles Huber goniometer.

Samples were produced by laser ablation of metal foils immersed in a thin film of water using a femtosecond laser (Hurricane, Spectra Physics). Droplets containing the suspended nanoparticles were deposited by means of a micropipette on a clean Si-wafer surface. For better distribution of the particles and for diminishing the hydrophobic character of the surface a small amount of ethyl alcohol was added to the sample. In Fig. 8 SEM micrographs of two different samples of Au nanoparticles generated under different ablation conditions are shown. The first sample was generated at high laser fluence

(above) while the second was produced at moderate fluence (below). The size distribution as well as the number of particles per volume deposited for analysis differs significantly. The diameter of nanoparticles of the first sample varies between 250 nm and less than 10 nm, those of sample two ranges between 70 nm and less than 10 nm. In both cases small particles cannot be characterised more accurately. Not only conglomerates of more than 20 particles (normal for the sample preparation used) are limiting the accuracy of the characterization, the limits of SEM resolution as well as the “transparency” of small particles for the electron beam impeded a more accurate determination of the diameter and a clear visualization of the morphology. Further, CdTe-nanoparticles and very high diluted Au-nanoparticles were investigated. The respective SEM micrographs are presented in Fig. 9 and Fig. 10. These two samples suffer from the same limitation mentioned before. However, clear agglomeration or conglomeration of particles can be observed for both samples leading to particles with an apparent larger diameter.

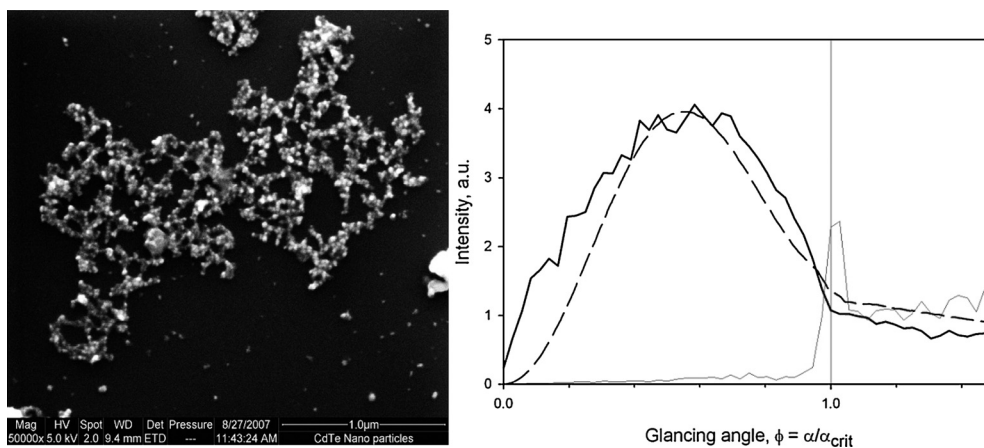


**Fig. 9** CdTe-nanoparticles of nominal 2–7 nm diameter after sample preparation for XSW SEM micrograph and XSW-scan (bold lines = DELTA current and footprint corrected XSW data, dashed line is a simulation using particles of 20 nm diameter) of particles and of a Cu contamination layer on top of the Si-wafer used as reflector.

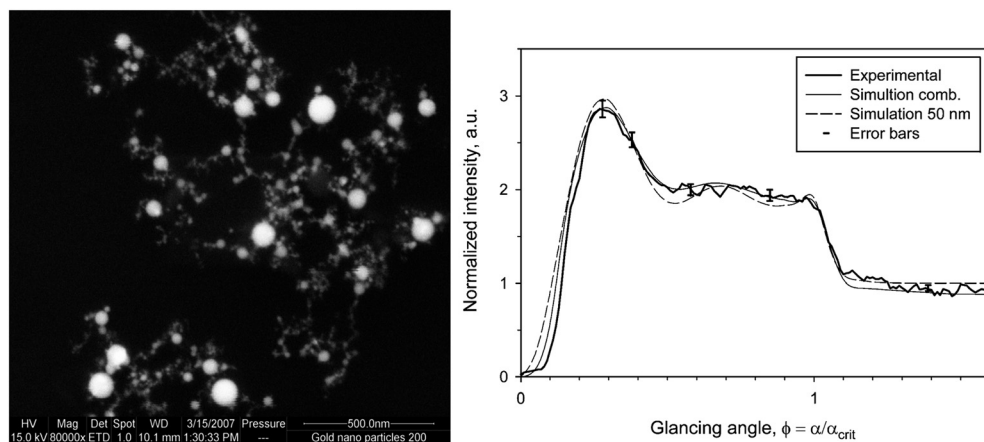


**Fig. 10** Gold nanoparticles characterized by XSW. Left: SEM micrograph representing a small selection of the area analyzed by XSW, right: measured XSW signal (bold line, error bars for counting statistics) and two simulation runs fitting the XSW-scan. It is possible to describe the measurement by only one particle size (50 nm diameter, dashed line) or by a linear combination of different particle sizes (e.g. 120 nm, 55 nm, 40 nm and 20 nm diameter, narrow full line) particles in black.

Grazing incidence XSW scans were performed at the beamline BL-9 of the DELTA synchrotron facility. A total counting time of one hour was chosen for each run at an excitation energy of 17.4 keV. The experimental set-up is presented in Fig. 2. In the upper representation the start position after optimal adjustment of the sample with respect to the beam is shown. The procedure of adjustment consists of a series of angle scans to place the reflector surface completely parallel to the exciting SR. Starting from this position step-scans with 160 single steps of  $0.001^\circ$  and a data acquisition time of 20 sec per point were selected for collecting the fluorescence radiation. This range of angular displacement insures a scan over a wide range of critical angles of total refraction. The step by step collected signals were plotted versus the glancing angle to obtain the XSW-spectra. A complete XSW-spectrum was collected within 60 minutes. Similar measurements were performed at BAMLine, BESSY II Synchrotron facility in Berlin, Germany.

## Results

The expected signals corresponding to XSW signals of nanoparticles could not be observed in the case of the two samples of Au nanoparticles shown in Fig. 8 left. The XSW scans obtained from these samples are represented in Fig. 8 right. The similarity of the recorded signals with the calculated signals for rough thin films is obvious.<sup>14</sup> The shape of the scans can be explained easily by the following model:

For normalized angles below  $\phi = (\alpha/\alpha_{\text{crit}})$  a primary and a reflected beam excite the sample to fluorescence the double excitation as it is known for TXRF. In both cases the surface of the reflector (Si-wafer) is covered by a more or less homogeneous film composed of different particles. No specific modulation of the signal can be attributed to single groups of particles and the result is more or less an average value. For angles  $\phi = (\alpha/\alpha_{\text{crit}}) > 1$  the intensities reach only the value of 1, which can be attributed to conventional XRF. On the other hand the field of standing waves should be seriously disturbed by the amount of sample presented for the analysis. A simple double excitation without modulated field is likely to be the excitation in these cases.

For samples with a less dense particle distribution per area, particularly expecting only a slightly disturbed field of X-ray standing waves, a more detailed and specific shape of the XSW-scans of different nanoparticles was observed. The first example (Fig. 9) shows the SEM micrograph of a partially agglomerated CdTe nanoparticles sample. The nominal particle size given by the deliverer is 2–7 nm powder (PlasmaChem GmbH, Berlin) for the material suspended in liquid. As shown in Fig. 9 the particles agglomerate after drying on a reflector. Next to the agglomeration several single particles can be observed. The corresponding XSW-scan shown on the right side of Fig. 9 contains the scan-data for the combined recorded counts for CdL- and TeL-lines (bold full line), the data of the numerical XSW simulation (dashed bold line) and the shape of the Cu signal (narrow line). According to the theory the Cu-signal of the XSW-scan can be attributed to a narrow (contamination) Cu-layer on the near surface region of the wafer.<sup>11</sup> On the other hand, the shape of the CdTe XSW-distribution differs significantly from those of Fig. 8. The attempt to fit the measured curve using the data calculated for nano-islands was negative. The recorded signal could only be

fitted when considering the equation for spherical particles. One single type of nanoparticle was found to fit the measured XSW-scan. The simulation using 20 nm spherical particles fulfil the conditions with certain accuracy. However, the result is not in agreement with the diameters ranging between 2 and 7 nm as given by the deliverer. The most convincing explanation when evaluating the SEM micrograph is the presence of agglomeration or conglomeration of particles: they suggest a bigger diameter. If a particle is a real single particle or an agglomeration or conglomeration of smaller particles cannot be decided by the method applied here. Additionally, it has to be mentioned that most particles are not a perfect sphere. They have to be assumed to be an intermediate object between nano-island and nanosphere. This fact can be taken into account for more precise calculations. The differences or deviations of the measured and the calculated XSW signal imply the presence of other particles or some particle size dependent effects, *e.g.* shadow from more extended agglomerations, matrix effects due to the heavy matrix of the particles.

In a second example, again for Au nanoparticles with highly diluted particle concentration, carefully distributed on the reflector surface, a more detailed shape of the XSW-scan was obtained. The SEM micrograph, the XSW-scan and the simulation of XSW signals are presented in Fig. 10. A clear spherical particle shape was obtained by the XSW-scan (*cf.* Fig. 5, right) and could be fitted in a first simulation run using only spherical particles of 50 nm diameters. The result seems to be reasonable; however, it was also possible to fit the scan using a linear combination of particles with diameters of 120 nm, 55 nm, 45 nm and 20 nm. A quantitative comparison between the results obtained by SEM and XSW is not reasonable when taking into account that the areas of inspection differ by more than 5 orders of magnitude. XSW uses about  $1 \text{ mm}^2$  while SEM shows only  $2.5 \mu\text{m}^2$ . However, the nanoparticles shown in the SEM micrograph range in the same order of magnitude as the results obtained by XSW analysis and simulation.

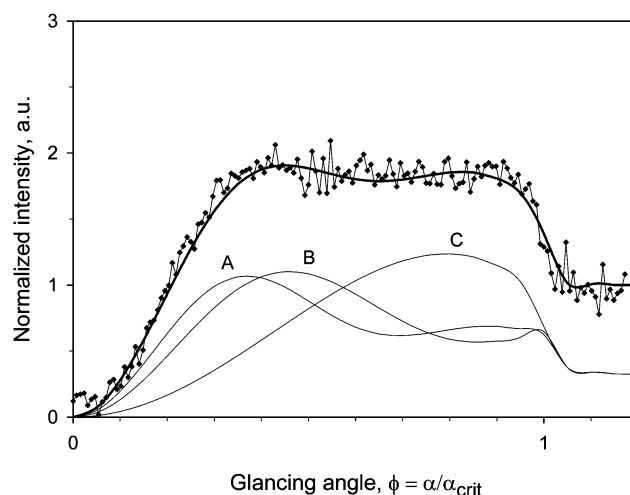


**Fig. 11** XSW scan of gold nanoparticles with nominal sizes between 88 nm and 45 nm. Numerical simulation of XSW signals assuming no restriction of the interference field caused by the finite coherence of primary radiation. The curve can be fitted using particles of (A) 36 nm, (B) 24 nm, and (C) 19 nm diameters with a relative abundance of 40%, 35%, and 25%, respectively.

The last example also concerns the characterization of gold nanoparticles produced by fs-laser ablation. The particles were size separated by means of aerodynamic impaction immediately after having been generated. A 13-stage low-pressure impactor (DLPI, Dekati, Tampere, Finland) was used for the size separation of small particulate matter. According to their aerodynamic diameter particles are separated into 13 groups with diameters of 2  $\mu\text{m}$ , 0.5  $\mu\text{m}$ , until 10 nm. We used the material deposited on stage 3 with a nominal size class containing particles between 88 and 45 nm aerodynamic diameters. SEM inspection of the samples collected in different stages show some irregularities in the separation process. Some large particles are transported to stages reserved for particles with nominal smaller diameters. Conglomerates of very fine particles were also detected in fractions of larger particles, while the diameters of the conglomerates correspond to the group size of the stage. However, the results of XSW scans performed on pieces of Si-wafers covered with particles collected at stage 3 are shown in Fig. 11. In the spectrum obtained at BESSY II a set of particles with different diameters (36 nm, 24 nm, and 19 nm with a relative frequency of 40%, 35%, and 25% respectively) could be used to fit the XSW signal.

## Conclusion

The finite coherence of X-rays involved in the process of total reflection of X-rays on a flat surface was considered for different excitation sources. The consequences for the expected field of standing waves above the reflector to be applied for X-ray Standing Waves measurements were discussed. Some limitations concerning the sample size in the dimension perpendicular to the reflector were established. Further, a form function for specific shaped particles was introduced in the calculations of XSW and allows a refined description of the experimental data. Consequently, a more precise fit of the numerical simulation with respect to the experimental data could be achieved. Some limitations concerning the excitation to X-ray fluorescence at grazing incidence conditions of the primary beam for small nanoparticles were described. These new deeper insights affect also the conventional TXRF measurements. However, most of the performed analyses can be accepted without changes. Only those samples with segregation or separation of single components into very small nanoparticles or nano-islands should be reconsidered and the results of quantification must be revised critically.

The proposed method for the characterization of nanoparticles in the recorded XSW-scan delivers an average value of the total number of irradiated particles which are in the field of vision of the detector. Even if the sensitivity is high, single nanoparticles cannot be accessed due to the low counting statistics. A small 1 nm diameter Au particle contains only about 30 atoms of gold while a 5 nm particle contains around 3800 atoms. This fact is also limiting the possibilities for a reliable

characterization by means of other techniques. The XSW method can be used as an independent reference measurement for the characterization of groups of particles with diameters ranging between 1 nm and 200 nm. For this purpose a special sample preparation is needed to produce a mono dispersely populated particle distribution over a large field of the reflector to avoid severe distortion of the X-ray standing wave field. The results of the numerical simulation are (in terms of size distribution and shape) not unambiguous, *e.g.* more than one solution can be presented to fit an XSW-scan. Nevertheless, the elemental composition and a possible particle size distribution are obtained in only a single run in a reasonable time. Precision and accuracy of the presented method cannot be assessed easily. If all system parameters are well known the deviations between measurement and simulation are of the order of 10%.

## Acknowledgements

The authors are indebted to the staff of BAMLine at BESSY II, especially to Martin Radtke and Bernd Müller for the support during control measurements, and to Metin Tolan and the DELTA staff for providing beam time at DELTA.

## References

- 1 R. Klockenkämper and A. von Bohlen, *J. Anal. At. Spectrom.*, 1992, **7**, 273–279.
- 2 D. K. G. de Boer, *Phys. Rev.*, 1991, **B44/2**, 498–511.
- 3 A. von Bohlen. Dissertation. TU-Dortmund, 2007.
- 4 J. Knoth, H. Schwenke and U. Weisbrod, *Spectrochim. Acta*, 1989, **B 44**, 477–481.
- 5 M. Krämer. Dissertation. TU-Dortmund, 2007.
- 6 M. Krämer, A. von Bohlen, C. Sternemann, M. Paulus and R. Hergenröder, *J. Anal. Atom. Spectrom.*, 2006, **21**, 1136–1142.
- 7 M. Krämer, A. von Bohlen, C. Sternemann, M. Paulus and R. Hergenröder, *Appl. Surface. Sci.*, 2007, **253**, 3533–3542.
- 8 H. A. Compton, *Philos. Mag*, 1923, **45**(270), 1121–1131.
- 9 Y. Yoneda and T. Horiuchi, *Rev. Sci. Instrum.*, 1971, **42**, 1069–1070.
- 10 <http://www.isas.de/fileadmin/img/pb4/pdf/TXRF-Publ-List.pdf>.
- 11 R. Klockenkämper. *Total-reflection X-ray fluorescence analysis*. John Wiley & Sons, Inc., New York (1997).
- 12 U. Reus and A. Prange, *Spectroscopy Europe*, 1993, **5**, 25–33.
- 13 P. Wobrauschek, *J. Trace and Microprobe Tech.*, 1995, **13/2**, 83–96.
- 14 R. Klockenkämper, J. Knoth, A. Prange and H. Schwenke, *Anal. Chem.*, 1992, **64**, 1115A–1123A.
- 15 C. Strelly, P. Wobrauschek, F. Meirer and G. Pepponi, *J. Anal. At. Spectrom.*, 2008, **23**, 792–798.
- 16 J. Als-Nielsen and D. McMorrow. *Elements of modern X-ray physics*. John Wiley & Sons, Inc., New York (2001).
- 17 M. J. Bedzyk, G. M. Bommarito and J. S. Schildkraut, *Phys. Rev. Lett.*, 1989, **62**, 1376–1379.
- 18 R. Klockenkämper and A. von Bohlen, *Spectrochim. Acta*, 1989, **B 44**, 461–469.
- 19 D. Hellin, W. Fyen, J. Rip, T. Delande, P. M. Mertens, S. De Gendt and C. Vinckier, *J. Anal. At. Spectrom.*, 2004, **19**, 1517–1523.
- 20 C. Krywka, C. Sternemann, M. Paulus, N. Javid, R. Winter, A. Al-Sawalmih, S. Yi, D. Raabe and M. Tolan, *J. Synchrotron Radiat.*, 2007, **14**, 244–251.